Journal of Non-Crystalline Solids 511 (2019) 115–124

Contents lists available at ScienceDirect

Journal of Non-Crystalline Solids

journal homepage: www.elsevier.com/locate/jnoncrysol

Modeling and experimental determination of physical properties of $Ge_xGa_ySe_{1-x-y}$ chalcogenide glasses II: Optical and thermal properties

Jason Lonergan[a,b,*], Charmayne Lonergan[c], John McCloy[b], Kathleen A. Richardson[a]

[a] College of Optics and Photonics, Department of Materials Science and Engineering, University of Central Florida, Orlando, FL 32816, USA
[b] School of Mechanical and Materials Engineering, Washington State University, Pullman, WA 99164, USA
[c] Energy and Environment Directorate, Pacific Northwest National Laboratory, 902 Battelle Blvd., Richland, WA 99352, USA

ABSTRACT

This study systematically analyzed the correlation between topological structure and chemical ordering on the optical and thermal properties of synthesized material in the glass forming region of the $Ge_xGa_ySe_{1-x-y}$ ternary. A series of ten compositions from 5 to 30 mol% Ge and 5 to 15 mol% Ga were examined within the ternary, showing broadband infrared properties with transmission from 1 to 25 μm. Topological constraint theory applied to compositions examined exhibited sharp inflection at the average coordination number of $< r > = 2.67$ defined as the chemical threshold where the glass network consists of tetrahedral $Ge(Ga)Se_2$ units. These observations indicate that thermal and optical properties in these chalcogenide glasses are highly sensitive to the chemical ratio of homopolar versus heteropolar bonds, Ge to Ga ratio, as well as the dimensionality of the topological structure. Glass transition and crystallization temperature values compare well with previous literature on similar Ge—X—Se systems. This is a comprehensive study that systematically examined thermal conductivity, heat capacity, absorption coefficient, and refractive index within the $Ge_xGa_ySe_{1-x-y}$ system, correlating these properties with structural network calculations. The presented methodology and findings will enable the compositional design of materials for infrared systems using $Ge_xGa_ySe_{1-x-y}$ glasses with broadband transmission.

1. Introduction

Chalcogenide glasses (ChGs) have primarily attracted research attention due to their infrared (IR) transmittance. In IR night vision technology, designs are based mainly on two regions in the electromagnetic spectrum, the mid-wave infrared (MWIR) 3–5 μm and long-wave infrared (LWIR) 8–12 μm. ChGs are non-oxide glasses that typically have large glass-forming regions which allow for tuning of physical properties over a range of compositions. The resulting glassy structure of each composition controls the physical properties; therefore, it is important to understand the structure-property correlations in order to design useful chalcogenide glasses.

Ge_xSe_{1-x} and $Ge_xGa_ySe_{1-x-y}$ glasses have been shown to consist of a covalently bonded network of elements in which the connectivity is controlled by atomic coordination numbers [1–5]. Phillips and colleagues have discussed the organization of covalent network glasses in terms of a balance of constraints and degrees of freedom [6–9]. A fundamental metric used to describe the covalent network topology is the average coordination number, denoted here as $< r >$ [10], a simple weighted sum of the element atomic fraction and its coordination number. Two important metrics are often observed in ChGs: the first, $< r > = 2.4$, represents the topological transition from a floppy to a rigid structure and the second, $< r > = 2.67$, represents the chemical threshold from a system with excess selenium to a selenium deficient one. Previous studies on glass transition temperatures (T_g) with respect to coordination number $< r >$ for various $Ge_xGa_ySe_{1-x-y}$ glasses show inflection at these two points [1,3,5,11,12]. A calculation of average bond energy $< E >$ has also been used to predict properties and evaluate compositional trends. T_g has been shown to correlate well with mean bond energy $< E >$ in covalent glasses, and was shown to relate to the activation energy for viscous flow in an Arrhenius viscosity Eq. (13) For further theoretical details employed in analyzing the structure within this glass system, see Part I of this paper [14] which relates structure to measured and modeled mechanical properties.

The purpose of this study was to systematically explore the property evolution of thermal and optical properties within the same ternary $Ge_xGa_ySe_{1-x-y}$ glass-forming compositional space (spanning $5 < x < 30$ Ge mol % and $5 < y < 15$ Ga mol %). In Part I of this two part series of papers, the background theory and mechanical properties measurements and predictions were supplied. In this Part II, trends in thermal and optical properties are reported versus $< r >$ using semi-empirical and theoretical calculations to elucidate mechanisms further. The findings realized through this complementary means of exploring the property evolution are compared, and further conclusions on the role of structure on properties are presented.

* Corresponding author.
E-mail address: jason.lonergan@pnnl.gov (J. Lonergan).

https://doi.org/10.1016/j.jnoncrysol.2019.01.034
Received 9 October 2018; Received in revised form 27 December 2018; Accepted 6 January 2019

2. Experimental procedures

2.1. Synthesis

Detailed synthesis procedures for the glasses examined have been described in Part I. Briefly, elemental starting materials (Ge: Alfa Aesar 5 N, Ga: Alfa Aesar 5 N, Se: Alfa Aesar 5 N) were placed in quartz ampoules in an inert glovebox, evacuated, and sealed. Ampoules were then heated to 800 °C for 12 h, then lowered to 750 °C, and then quenched to room temperature with forced air. Two batches were processed for each composition. For property testing, glasses were annealed for 12 h at T_g - 40 °C to ensure structural glass relaxation. The 10 mm diameter glass rods were cut using a diamond edge saw blade, and ground and polished into slices for thermal and optical property measurement, or crushed to a powder using a mortar and pestle for thermal analysis. Experimental error was determined as the standard deviation of the average of at least three measurements for every data point. In the case where a data point was derived from multiple measurements each having their own uncertainty, a propagation of uncertainties calculation was followed according to J. R. Taylor [15].

2.2. Thermal properties

The glass transition temperature, thermal expansion coefficient, thermal conductivity, and heat capacity were experimentally determined to aide in understanding each glass' structural and chemical arrangement.

The glass transition temperature (T_g) and crystallization temperature (T_x) of each $Ge_xGa_ySe_{1-x-y}$ glass was measured by a Netzch (DSC F1 Phoenix, Boston, MA) differential scanning calorimeter (DSC) on powders of each sample, ground using a mortar and pestle. In a sealed aluminum pan, approximately 20 mg of glass powder was heated at a rate of 10 °C/min in the DSC. The inflection point (the minima or maxima of the first derivative) of the endotherm in the heat flow curve was taken as the glass transition temperature.

The transient plane source (TPS) method (ThermTest, TPS 3500, Fredericton Canada) was used to measure overall thermal conductivity (k_T) and specific heat capacity (c_v) [16]. Specimens were cut from bulk glass rods to a nominal thickness of 2.5 mm and polished to 0.05 μm roughness. The TPS sensor acts as both a heat source and resistance thermometer. As electric power is supplied to the sensor, the increase in mean temperature ($T(\tau)$) of the specimen can be directly related to the variation in the sensor resistance $R(T)$ as [16]

$$R(T(\tau)) = R_0[1 + \alpha_T(T(\tau) - T_0)] \tag{1}$$

where R_0 is the initial resistance at T_0, the initial temperature, and α_T is the temperature coefficient of resistance (TCR). The TCR α_T can be solved using Eq. (1) and the following expression for mean temperature of the sensor,

$$T(\tau) = \frac{P_i}{\pi^{3/2} r_s k_T} D(\tau) \tag{2}$$

where P_i is the input power, r_s is the radius of the sensor, and $D(\tau)$ is a shape function which has the following form, Eq. (3), where τ is time.

$$D(\tau) = \sqrt{\frac{t \cdot D_T}{a^2}} \tag{3}$$

Thermal diffusivity, D_T, can be obtained by utilizing a plot of the recorded temperature versus $D(\tau)$. The specific heat capacity is also calculated indirectly with Eq. (4),

$$c_v = \frac{k_T}{D_T} \tag{4}$$

Step-wise, pulsed heating (of power = 10 mW and pulse length = 0.1 s) were used to generate the resistively measured temperature response curves. A minimum of five tests were performed for each data point and the standard deviation is noted by the error bars shown (no observable error bars indicates the error was within the data point). c_v was converted to c_p through division by the measured specimen's density (ρ) (details on density measurements and data in Part I).

2.3. Optical properties

As these glasses are intended to be considered for use as IR optical components, the determination of their optical properties was crucial. Transmission (t) was obtained from the ultraviolet through the mid-infrared, with both Fourier Transform Infra-Red (FTIR) (Thermo Scientific Nicolet is5) and UltraViolet-Visible (UV–Vis) spectroscopy (Cary 500 UV–Vis-NIR Spectrophotometer), where background spectra were subtracted to account for ambient H_2O and CO_2. Refractive index, n, was independently measured in the mid-infrared at 4.515 μm. The vibrational structure of the glasses as measured using Raman spectroscopy was reported in Part I. For these techniques, the 10 mm diameter bulk glass rods were cut into nominally 2.0 mm thick slices, ground, and then polished to a 0.5 μm finish.

Refractive index was measured at a wavelength of 4.515 μm using a Metricon model 2010 M prism coupling system, at room temperature. Measurements were performed by holding samples in contact with a single crystal Ge prism. The refractive index was measured ten times to obtain an average with relative error ± 0.0003 refractive index units. Details of the Metricon system [17,18], and its application to index measurements in ChG [17] can be found in the literature.

The absorption coefficient at room temperature was both theoretically and experimentally determined using measured refractive index, thickness, and transmission values. For intrinsic structure-property comparisons based on coordination number, the theoretical values were used. For thermal property calculations, the experimental values where used in order to avoid overestimation of phonon conduction by inclusion of phonons that do not make it through the sample due to a scattering or reflection mechanism. The theoretical transmittance (T) was calculated at 4.515 μm and estimated across the full spectrum using the following Fresnel equation to account for internal reflection losses.

$$T = \frac{4 n_t n_i}{(n_t + n_i)^2} \tag{5}$$

In Eq. (5), n_i is the refractive index of the incident wave, and n_t is the refractive index of the transmitted wave. Since we measure refractive index in air, $n_i \approx 1$ and n_t is the measured refractive index of the given glass composition. The transmittance was then converted to absorbance (A) using Eq. (6),

$$A = \log_{10}\left(\frac{1}{T}\right) \tag{6}$$

and the absorption coefficient, $\alpha(\mathrm{cm}^{-1})$, was then related to absorbance by the relation shown in Eq. (7),

$$\alpha = \frac{A}{l} \tag{7}$$

where l is the thickness of the specimen. For experimental determination of absorption coefficient, absorbance was calculated using Eq. (8) as shown below, and then converted to absorption coefficient using Eq. (7).

$$A = 2 - \log_{10}(\%t) \tag{8}$$

3. Results and discussion

3.1. Glass transition temperature

Fig. 1 shows the glass transition temperature of the $Ge_xGa_ySe_{1-x-y}$ compositions versus $< r >$. The glass compositions that formed bulk glass (as defined in Part I), their equivalent coordination number, and

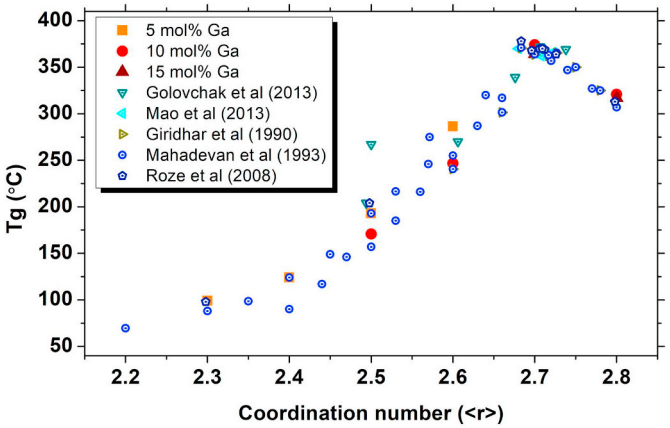

Fig. 1. Measured glass transition temperatures (T_g) with respect to coordination number < r > for various $Ge_xGa_ySe_{1-x-y}$ glasses for the current work compared to literature values [1,3,5,11,12]. Error bars are within the data points.

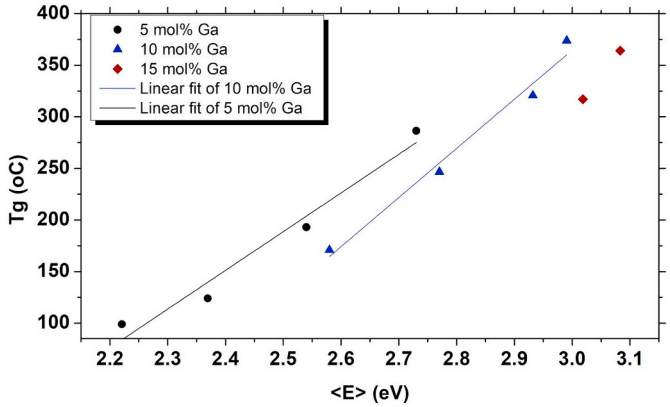

Fig. 2. Glass transition temperatures, T_g, of $Ge_xGa_ySe_{1-x-y}$ glasses with respect to calculated mean bond energies < E > . Linear trend lines have been fit to the series with > 3 or more data points (i.e., 5 mol% and 10 mol% data sets). Error bars are within the data points.

measured characteristic properties are reported in Table 1. The lowest T_g for the current work was found to be 99 °C for $Ge_{0.1}Ga_{0.05}Se_{0.85}$ ($< r > = 2.3$) whereas the highest T_g was 347 °C for $Ge_{0.25}Ga_{0.1}Se_{0.65}$ ($< r > = 2.7$). A maximum is observed at $< r > = 2.67$ and a small inflection is seen at $< r > = 2.4$. The values measured in this study compare well with those previously reported in literature (Fig. 1). There does not appear to be any discernable trend regarding the ratio of Ge to Ga for compositions with similar coordination numbers, other than that the role of Ga in the network for a given average bond energy tends to lead to a reduced transition temperature, suggesting some network depolymerization with its addition.

Fig. 2 shows the T_g of the $Ge_xGa_ySe_{1-x-y}$ compositions versus the mean atomic bonding energy, < E > . Values range from 2.2 to 3.1 eV with increasing bond energy associated with increasing Ge(Ga)—Se bonds. The highest T_g is measured for compositions with the nominally heteropolar bonding and, in general, T_g increases with increasing < E > . For the two data series with three or more data points, a linear relation is observed. The 5 and 10 mol% series have a linear fit with R^2 values of 0.95 and 0.97, respectively. This equates to compositions with the lowest absolute selenium deficiency (defined in Appendix B) as shown in Table 1. It can also be seen that glasses with identical < r > values, but higher ratios of Ga to Ge, exhibit higher T_g's.

3.2. Optical

Fig. 3a shows optical transmission spectra of the $Ge_xGa_ySe_{1-x-y}$ compositions. The majority of the glasses tested exhibit broadband transmission from ~1000 to ~17,000 nm. Maximum transmission values around 60% are consistent with those observed in the literature for similar $Ge_xGa_ySe_{1-x-y}$ and $Ge_xGa_ySe(S)_{1-x-y}$ glasses [12,20,21]. $Ge_{0.10}Ga_{0.5}Se_{0.85}$ and $Ge_{0.25}Ga_{0.15}Se_{0.60}$ have significantly lower maximum transmission values due to the presence of large crystallites within the glass (detected by XRD, not shown) causing wavelength independent, large particle scattering. Fig. 3b shows a blue-shift as coordination numbers increase from $< r > = 2.4$ to 2.7, which agrees with the theoretical Fresnel losses based on measured refractive index. A large absorption band can be observed around 12.5 μm, attributed to the impurity absorption of the Ge—O bond [20]. The small absorption bands observed near 3 μm and 4.2 μm have been reported to be due to O—H and Se—H impurities [21]. Although several impurity bands are observed, 90% of the compositions have acceptable transmission (~90% of maximum) for one of the two IR bands (3–5 or 8–12 μm) used in industry night vision equipment, and seven out of the ten glasses exhibit broadband infrared transmission covering both regimes. It should be noted that no effort was made to explicitly purify these glasses beyond keeping the elemental starting powders in a dry N_2 purged glove box. This confirms that the $Ge_xGa_ySe_{1-x-y}$ chalcogenide glass system is a promising glass-forming regime for infrared optical systems.

Fig. 4 shows the calculated absorption coefficients for $Ge_xGa_ySe_{1-x-y}$ compositions using measured values of refractive index and transmission; these values can also be found in Table 2. There is a clear trend with overall absorption coefficients increasing with increasing Ga content for compositions with a similar $< r > $. A second trend is also observed, in which the absorption coefficient decreases for each Ga mol % series, as the coordination number $< r > = 2.67$ is approached. Although measurement error was significant (mostly due to uncertainty of measurement of specimen thickness and slight residual wedge within polished discs), overall trends are larger than the error values for the first and last data point in each Ga mol % series.

Fig. 5 shows absorption coefficient versus < E > for $Ge_xGa_ySe_{1-x-y}$ compositions from $< E > = 2.37$ to 3.0. The same eight compositions

Table 1
Summary of characteristic properties of $Ge_xGa_ySe_{1-x-y}$ glass compositions. T_g and T_x are the temperatures of the glass transition and crystallization, respectively, and their difference is ΔT. < r > is the glass coordination number and S is the selenium deficiency (defined in Appendix B).

Ge (at_f)	Ga (at_f)	Se (at_f)	< r >	S	< E >	T_g (°C)	T_x (°C)	ΔT
0.10	0.05	0.85	2.3	−1.8	2.22	99 ± 3.9		
0.15	0.05	0.80	2.4	−1.0	2.37	124 ± 2.4	291 ± 4.6	167
0.20	0.05	0.75	2.5	−0.5	2.54	193 ± 4.7	379 ± 3.8	186
0.25	0.05	0.70	2.6	−0.2	2.73	286 ± 5.0	435 ± 2.4	148
0.15	0.10	0.75	2.5	−0.5	2.58	171 ± 4.3	307 ± 3.1	136
0.20	0.10	0.70	2.6	−0.2	2.77	247 ± 3.3	392 ± 4.2	146
0.25	0.10	0.65	2.7	0.1	2.99	374 ± 5.6	489 ± 5.1	115
0.30	0.10	0.60	2.8	0.3	2.93	321 ± 4.9	423 ± 2.8	102
0.20	0.15	0.65	2.7	0.1	3.08	364 ± 4.1	437 ± 3.7	73
0.25	0.15	0.60	2.8	0.3	3.02	317 ± 2.8	377 ± 5.4	60

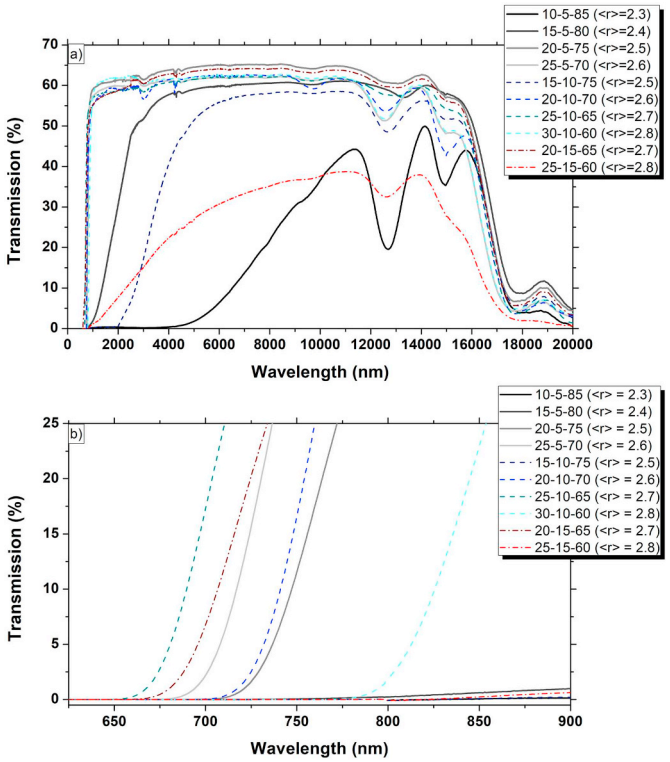

Fig. 3. Transmission for $Ge_xGa_ySe_{1-x-y}$ compositions ranging from $< r > = 2.3$ to 2.8 over the entire spectral range (a) from 0 to 20,000 nm and (b) for the lower wavelength cut-on transmission edges from 625 to 900 nm. Thickness for the tested specimens was 2.0 mm ± 0.2. The 5 mol% Ga series is in shades of gray with solid lines, 10 mol% Ga series is in shades of blue with a dashed line, and 15 mol% Ga series is in shades of red with a dashed-dot line. (For interpretation of the references to colour in this figure legend, the reader is referred to the web version of this article.)

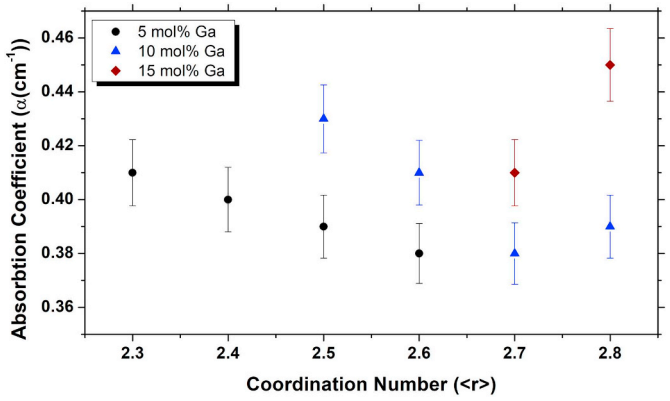

Fig. 4. Absorption coefficient for $Ge_xGa_ySe_{1-x-y}$ versus coordination number from $< r > = 2.4$ to 2.8. Absorption coefficients were calculated at $\lambda = 4.515$ μm.

were analyzed as was done for comparisons between absorption coefficient and $< r >$. Direct linear trends are observed with R^2 values of 0.996 and 0.999 for 10 mol% Ga and 5 mol% Ga respectively. A decrease in absorption coefficient with increasing average bond energy is seen for all compositions. For compositions with similar $< E >$, a higher ratio of Ga to Ge results in a higher absorption coefficient. Although the measurement error was large, the error bars for the lowest $< E >$ composition are outside of the error bars for the highest $< E >$ composition.

Once the transmission and absorption coefficient values were determined, the optical band gap was determined using the 'non-direct transition' model proposed by Tauc [22,23]. Due to previous research on Ge_xSe_{1-x} glasses, it was assumed that all the $Ge_xGa_ySe_{1-x-y}$ compositions in this study have an indirect band gap [24]. For that reason, $r = 2$ was used in Eq. (9), the correlation between optical band gap, absorption coefficient, and bond strength [13,23,25–27],

$$\alpha\hbar\omega = B(\hbar\omega - E_g)^r \quad (9)$$

where E_g is the optical energy gap, B is a constant called the Tauc slope, ω is the angular frequency, and $\hbar$ is the reduced Planck's constant.

Fig. 6a shows the Tauc plot of the absorption coefficient values. The optical band gap is determined by a linear extrapolation of the high energy data to the x-axis (energy). The low-energy values are nearly identical for all the compositions except $Ge_{0.15}Ga_{0.10}Se_{0.75}$ and $Ge_{0.15}Ga_{0.05}Se_{0.80}$. Fig. 6b is a plot of the photon energies determined by the intersection of the linear and the calculated optical band gap values, generated from the Tauc plot, with respect to the corresponding compositions coordination number. These results are in agreement with what has been observed in the literature for similar systems; for instance, Tanaka and Lucovsky have observed increases in optical band gap from $< r > = 2.4$ to 2.67 for Ge_xSe_{1-x} glass compositions [28,29].

Fig. 7 shows the refractive index at $\lambda = 4.515$ μm of the $Ge_xGa_ySe_{1-x-y}$ compositions plotted against their respective coordination numbers. An increase in refractive index is seen as coordination number move away from $< r > = 2.7$. Compositions with similar $< r >$ but higher ratios of Ge to Ga exhibit a higher refractive index. Similar trends were found in the literature by Wei in $Ge_xSb_ySe_{1-x-y}$ glasses [30]. In addition, there is a steeper slope for the composition with excess Ge(Ga), $< r > > 2.67$, compared to those with excess Se, $< r > < 2.67$. The explanation for this trend is fairly straightforward, as refractive index has been shown to directly correlate to electronic density. In the case of Se-deficient glasses, $< r > > 2.67$, both energy and density increase which should lead to greater electronic density [2].

3.3. Thermal

Fig. 8 shows the measured heat capacity of the $Ge_xGa_ySe_{1-x-y}$ series versus the average coordination number. Values increase from 0.261 J/g·K for $Ge_{0.10}Ga_{0.05}Se_{0.85}$ ($< r > = 2.3$) to 0.305 J/g·K for $Ge_{0.25}Ga_{0.15}Se_{0.60}$ ($< r > = 2.8$). Similar trends have been observed in Ge_xSe_{1-x} glasses from $< r > = 2.3$ to 2.8 [31,32]. Calculated heat capacities for all $Ge_xGa_ySe_{1-x-y}$ compositions are shown in Fig. 8 and listed in Table 3. These values range from 0.231 to 0.276 J/g·K and increase with increasing coordination number similar to measured values. An exact solution for the Debye function, which was used to calculate the heat capacity, can be found in Appendix A. Calculated values for Debye temperature (θ_D) are found in Table 3 showing that θ_D varied from 288 to 344 K. Although the measured values are higher than those predicted by Debye theory, with a maximum difference of ~20% at $< r > = 2.3$, an increase in heat capacity with increasing coordination number is observed in both data sets. The measured values are most likely lower due to the assumption that acoustic velocities are identical to phonon vibrational frequencies. Although close, the acoustic velocities measure less due to defects within the bulk sample and do not exactly represent the defect-free phonon vibrations.

Fig. 9 shows the thermal conductivity versus the coordination number for the $Ge_xGa_ySe_{1-x-y}$ series. Values increase with increasing coordination number with a minimum of 0.186 W/m·K measured for $Ge_{0.10}Ga_{0.5}Se_{0.85}$ ($< r > = 2.3$) and a maximum of 0.313 W/m·K measured for $Ge_{0.25}Ga_{0.15}Se_{0.60}$ ($< r > = 2.8$). This represents ~40% increase in thermal conductivity from $< r > = 2.3$ to 2.8. For compositions with similar coordination numbers, there appears to be a slight increase with higher ratios of Ga to Ge. Although these shifts are small, in most cases they are outside of the error bars, which are within the data points for almost all the measurements. In addition, the increase in

Table 2
Summary of measured physical properties of $Ge_xGa_ySe_{1-x-y}$ glass compositions; at_f is atomic fraction.

Ge (at_f)	Ga (at_f)	Se (at_f)	< r >	n	α_{AVG} (cm^{-1})	k_T (W/m·K)	c_p (J/g·K)
0.10	0.05	0.85	2.3	2.454 ± 0.001	1.68 ± 0.15	0.186 ± 0.002	0.261 ± 0.002
0.15	0.05	0.80	2.4	2.432 ± 0.002	1.23 ± 0.09	0.191 ± 0.001	0.265 ± 0.005
0.20	0.05	0.75	2.5	2.412 ± 0.003	1.06 ± 0.13	0.209 ± 0.002	0.269 ± 0.001
0.25	0.05	0.70	2.6	2.387 ± 0.002	0.88 ± 0.17	0.227 ± 0.002	0.275 ± 0.005
0.15	0.10	0.75	2.5	2.432 ± 0.003	1.77 ± 0.09	0.212 ± 0.002	0.276 ± 0.005
0.20	0.10	0.70	2.6	2.404 ± 0.001	1.32 ± 0.13	0.226 ± 0.003	0.276 ± 0.005
0.25	0.10	0.65	2.7	2.367 ± 0.004	0.91 ± 0.08	0.264 ± 0.001	0.282 ± 0.002
0.30	0.10	0.60	2.8	2.528 ± 0.003	1.05 ± 0.10	0.300 ± 0.002	0.297 ± 0.004
0.20	0.15	0.65	2.7	2.380 ± 0.001	1.38 ± 0.08	0.267 ± 0.001	0.287 ± 0.004
0.25	0.15	0.60	2.8	2.544 ± 0.002	2.45 ± 0.23	0.313 ± 0.002	0.305 ± 0.003

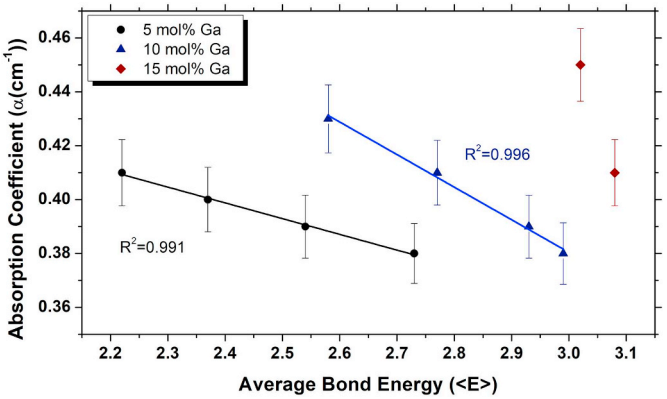

Fig. 5. Absorption coefficient of $Ge_xGa_ySe_{1-x-y}$ compositions at λ = 4.515 μm with respect to < E > from 2.2 to 3.1.

thermal conductivity does not exhibit a linear trend, but rather, something closer to a polynomial increase with coordination number. The real trend is probably not a continuous change with coordination but rather small inflection shifts at the $< r > = 2.4$ and 2.67 transition regimes followed by relatively linear behavior elsewhere.

Lattice and photonic portions of total thermal conductivity were calculated as shown in Fig. 10 using gas kinetic theory (Eq. (A-1 & 2)). The lowest lattice conductivity value of 0.059 W/m·K was calculated for $Ge_{0.10}Ga_{0.5}Se_{0.85}$ ($< r > = 2.3$) and the highest value of 0.18 W/m·K was calculated for $Ge_{0.25}Ga_{0.15}Se_{0.60}$ ($< r > = 2.8$). This represents a change of ~67% in lattice thermal conductivity from $< r > = 2.3$ to 2.8. Perhaps more surprising than the large shift in calculated lattice conduction is the large percentage of photon conduction found at room temperature for all compositions. Photonic thermal transport was responsible for ~40 to 75% of the overall thermal conductivity across all the compositions. Photonic thermal conductivity ranged from 0.075 W/m·K at $< r > = 2.3$ to 0.168 W/m·K at $< r > = 2.6$. Values decreased as coordination number moved away from the chemical ordering threshold of $< r > = 2.67$.

4. Discussion

4.1. Glass transition temperature trends

The possible slight inflection at $< r > = 2.4$ in the T_g as shown in Fig. 1 indicates that the glass transition temperature is influenced by the topological structure, and that as the system moves from 1-D chain-like structure to a 2-D cross-linked structure, and the atoms becomes more interconnected and resistant to bond breakage and reorganization due to increasing temperature. The highest value and inflection point, found at $< r > \approx 2.67$, correlates to a structure comprised of edge- and corning-sharing $Ge(Ga)Se_{4/2}$ tetrahedra, which was verified at this coordination in Part I [2,3,33–35]. This point is known as the chemical ordering threshold, which indicates a dominant presence of heteropolar

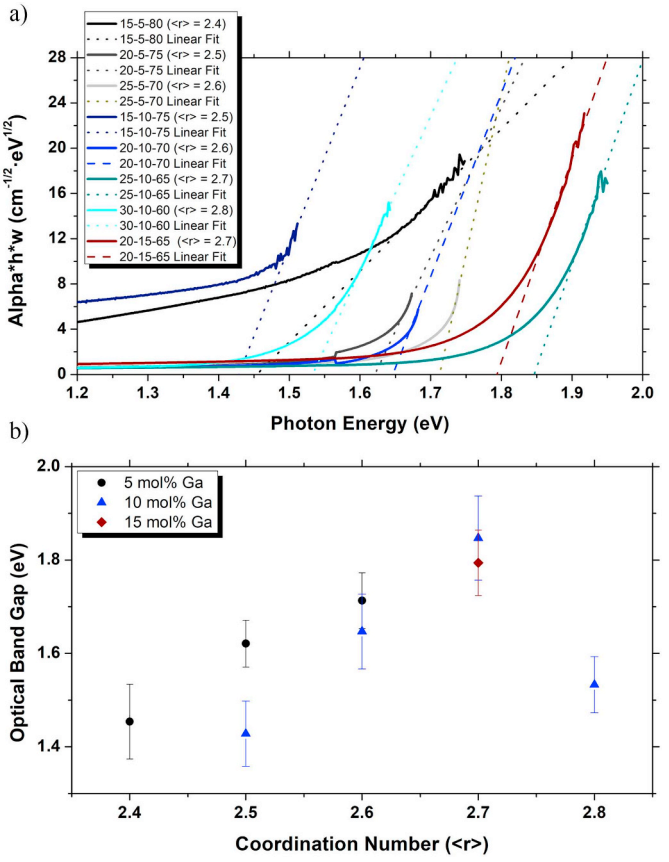

Fig. 6. (a) Tauc plot were the solid lines represent the measured experimental data and dashed lines represent the linear fits of the high energy regions; (b) calculated optical band gaps using the linear fits.

bonds. Therefore, glass transition temperature in the $Ge_xGa_ySe_{1-x-y}$ system is affected by both topological ordering and chemical thresholds simultaneously. In addition, ΔT (Table 1) exhibits an inverse trend with *S*, suggesting that the glass instability is driven by the Se deficiency in the network. This makes intuitive sense, as Se is the glass former and Ge (Ga) are network modifiers. Increasing the ratio of network modifier to glass formers, in theory, would lead to a glass with a lower activation energy to crystallization.

Physical properties such as T_g can also be connected to the mean atomic bonding energies of the glass structure as shown in Fig. 2. The increase in the glass transition temperature can be attributed to the higher bond energy of heteropolar, as opposed to homopolar, bonds. As the Ge(Ga) content increases, four-fold coordinated Ge(Ga) atoms ($U_{Ge-Se} = 2.12$ and $U_{Ga-Se} = 2.32$ eV) substitute for two-fold coordinated Se atoms ($U_{Se-Se} = 1.9$ eV), which increases the crosslinking and average bonding energy, resulting in an increase in T_g [13]. Further addition of

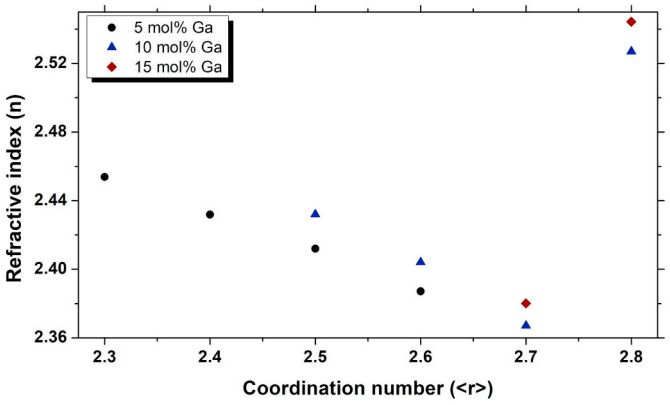

Fig. 7. Refractive index for the $Ge_xGa_ySe_{1-x-y}$ series at $\lambda = 4.515\,\mu m$ with respect to coordination numbers from $< r > = 2.3$ to 2.8. Error bars are within the data points.

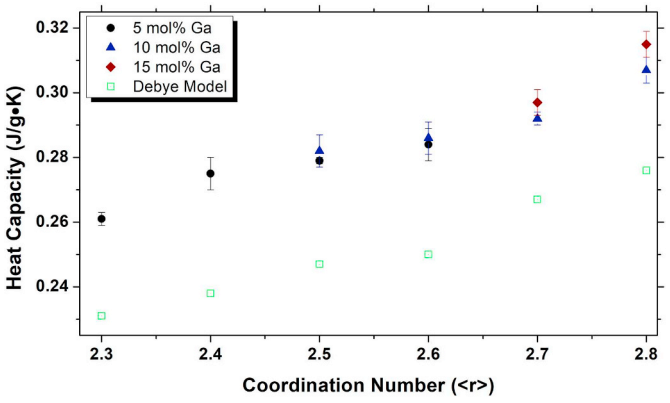

Fig. 8. Measured heat capacity values for $Ge_xGa_ySe_{1-x-y}$ system with respect to coordination numbers from $< r > = 2.3$ to 2.8. Also shown is the calculated value of heat capacity based on the Debye model.

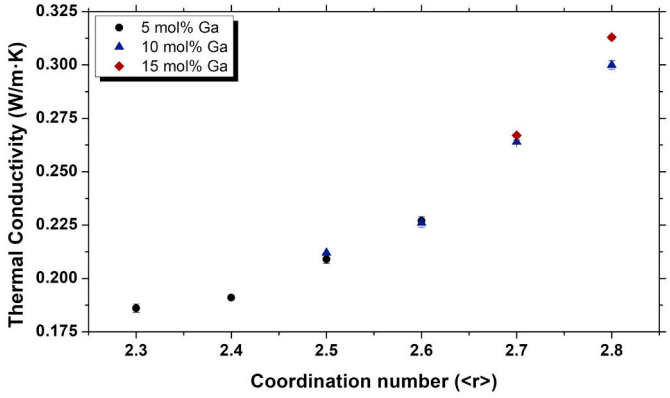

Fig. 9. Measured total thermal conductivity using the TPS method with respect to coordination numbers from $< r > = 2.3$ to 2.8. Error bars are found within the data points.

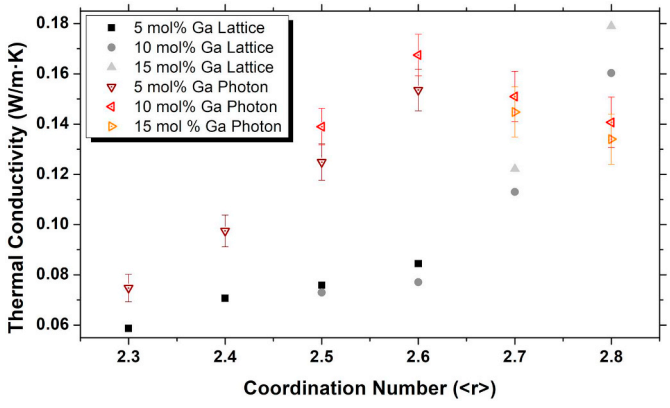

Fig. 10. Breakdown of lattice and photon thermal conduction mechanisms in $Ge_xGa_ySe_{1-x-y}$ series with respect to coordination number from $< r > = 2.3$ to 2.8. Lattice conduction is shown in shades of gray and solid symbols, and photon conduction is shown in shades of red with open symbols (colors refer to the online version of the article). (For interpretation of the references to colour in this figure legend, the reader is referred to the web version of this article.)

Ge(Ga) atoms and removal of Se results in the formation of homopolar Ge(Ga)—Ge(Ga) bonds, where $U_{Ge\text{-}Ge} = 1.63$, $U_{Ga\text{-}Ga} = 1.48$ eV, and $U_{Ge\text{-}Ga} = 1.60$ eV. The reduction in average bond energy means less thermal energy is required to break bonds and reorganize the structure, and results in a reduced T_g. The bonding changes discussed so far were indeed measured and confirmed to agree with topological constraint theory in Part I. For instance, compositions of $< r > < 2.67$ had large Se—Se vibrational peaks, Ge(Ga)—Se tetrahedral vibrations increased as compositions approached $< r > = 2.67$, and Ge(Ga)—Ge(Ga) cage-like units were detected in Se deficient compositions, $< r > > 2.67$. Average bond energy calculations have shown that, regardless of the network dimensionality of any given glass composition, the glass transition temperature in the $Ge_xGa_ySe_{1-x-y}$ system is strongly influenced by chemical ordering.

4.2. Absorption and band gap trends

Considering optical absorption, and taking the 10 mol% Ga data set as a representative series, a value of $1.00\,cm^{-1}$ was observed for $Ge_{0.15}Ga_{0.10}Se_{0.75}$ ($< r > = 2.5$), a minimum of $0.79\,cm^{-1}$ was measured for $Ge_{0.25}Ga_{0.10}Se_{0.65}$ ($< r > = 2.7$), and an increase to $0.86\,cm^{-1}$ was observed for $Ge_{0.30}Ga_{0.10}Se_{0.60}$ ($< r > = 2.8$). The

Table 3
Summary of calculated and theoretical optical, thermal, and mechanical properties for $Ge_xGa_ySe_{1-x-y}$ glass compositions. Values that were not measured are denoted with a NM.

Ge (at_f)	Ga (at_f)	Se (at_f)	< r >	E_d (eV)	E_o (eV)	E_g (eV)	$\theta_{D,\,theo}$ (K)	$c_{p,\,theo}$ (J/g·K)	$K_{l,\,calc}$ (W/m·K)	$K_{p,\,calc}$ (W/m·K)
0.10	0.05	0.85	2.3	21.78 ± 0.001	4.417 ± 0.001	NM	231	0.231	0.100	0.075 ± 0.005
0.15	0.05	0.80	2.4	21.55 ± 0.002	4.463 ± 0.002	1.45 ± 0.08	243	0.238	0.098	0.084 ± 0.006
0.20	0.05	0.75	2.5	21.4 ± 0.003	4.521 ± 0.003	1.62 ± 0.05	254	0.247	0.084	0.125 ± 0.007
0.25	0.05	0.70	2.6	21.31 ± 0.002	4.613 ± 0.002	1.71 ± 0.06	265	0.250	0.074	0.154 ± 0.008
0.15	0.10	0.75	2.5	21.96 ± 0.003	4.548 ± 0.003	1.43 ± 0.07	259	0.247	0.073	0.139 ± 0.007
0.20	0.10	0.70	2.6	21.78 ± 0.001	4.636 ± 0.001	1.65 ± 0.08	257	0.250	0.059	0.168 ± 0.008
0.25	0.10	0.65	2.7	21.65 ± 0.004	4.781 ± 0.004	1.85 ± 0.09	299	0.267	0.113	0.151 ± 0.01
0.30	0.10	0.60	2.8	21.55 ± 0.003	4.074 ± 0.003	1.53 ± 0.06	339	0.276	0.160	0.141 ± 0.01
0.20	0.15	0.65	2.7	22.04 ± 0.001	4.803 ± 0.001	1.79 ± 0.07	312	0.267	0.122	0.145 ± 0.008
0.25	0.15	0.60	2.8	21.9 ± 0.002	4.079 ± 0.002	NM	355	0.276	0.179	0.134 ± 0.009

inflection near < r > = 2.67 is most likely due to the chemical ordering threshold. This suggests that heteropolar Ge(Ga)—Se bonds absorb less incident electromagnetic radiation than homopolar Ge(Ga)—Ge(Ga) or Se—Se bonds; in other words, there is an inverse relation between how tightly an atom is bound to its nearest neighbors (as indicated by the bond strength) and its interaction with incident electromagnetic radiation in the infrared within the $Ge_xGa_ySe_{1-x-y}$ system.

The linear trend observed when absorption coefficient is plotted versus average bond energy (Fig. 5) indicates that this property is more directly affected by the strength of the individual bonds than by the larger scale topological ordering of the material. The fact that the linear trends between 5 mol% Ga and 10 mol% Ga show different slopes, and different values for similar < E > , is most likely due to topological differences between the structure of the Ge and Ga tetrahedra. A possible explanation for this could be due to the valence structure of Ga which only has three electrons to readily donate to the $GaSe_2$ unit, and charge balance may result in some form of orbital hybridization which could result in a kinked or altered tetragonal structure compared to $GeSe_2$. Regardless of the role the topological structure plays between Ge and Ga tetrahedra, the dominant factor determining overall absorption coefficient trends within the $Ge_xGa_ySe_{1-x-y}$ system appears to be average bond strength.

The reason for the increase in the low energy y-axis values in Fig. 6a (Tauc plot) for $Ge_{0.15}Ga_{0.10}Se_{0.75}$ and $Ge_{0.15}Ga_{0.05}Se_{0.80}$ is due to the higher wavelength cut-on values for these two compositions caused by wavelength dependent scatter from nano-crystals. The inverse trend of the optical band gap, E_g (Fig. 6b), compared to absorption coefficient, α (Fig. 4), can be explained by the correlation between optical band gap, absorption coefficient, and bond strength as shown in Eq. (9). This indicates that the absorption coefficient should decrease as E_g increases. Therefore, optical band gap should increase with increasing average bond strength, as is observed for the $Ge_xGa_ySe_{1-x-y}$ compositions in this study.

The minimum found at $< r > = 2.7$ for refractive index indicates that “homopolar” bonds of either Se—Se or Ge(Ga)—Ge(Ga) interact more strongly with incident electromagnetic radiation (producing polarization) than “heteropolar” Ge(Ga)—Se bonds predominantly present at this point. The steeper slope for glasses with Ge(Ga)—Ge(Ga) bonding suggests that metal-metal bonds have a much stronger effect on refractive index than Se—Se bonds, despite the chalcogen ion's higher polarizability. Further elucidation of the mechanics behind refractive index can be found in the single oscillator model proposed by Wemple and DiDomenico [36,37], as shown in Eq. (10):

$$n^2 - 1 = (E_d E_0)/(E_0^2 - E^2) \tag{10}$$

where n is the refractive index, E_0 is the energy of the effective dispersion oscillator, E is the photon energy, and E_d is the dispersion energy. For this study, E is a constant since all refractive index measurements were performed at a single wavelength, $\lambda = 4.515\,\mu m$. E_d was calculated with the following Equation [36,37],

$$E_d = \beta N_c Z_a N_e \tag{11}$$

where β is a parameter equal to 0.26 eV for ionic bonding and 0.37 eV for covalent bonding, N_c is the coordination number of the nearest neighbor cations to the anion, Z_a is the chemical valence of the anion, and N_e is the total number of electrons per bonding pair [36,37]. Calculated values of E_d and E_0 can be found in Table 3. E_d is roughly four times the size of E_0 for all compositions and decreases as < r > increases for all compositions. A maximum is observed for E_0 at < r > = 2.7, and values continually decrease as coordination number moves away from this value. These trends are consistent with those observed in the literature [28,29]. Typically, E_0 is considered a measure of the average bond energy of the chemical bonds present in the material [22]. It then makes sense that E_0 increases approaching the < r > = 2.7 chemical threshold due to the increasing presence of stronger (Ga)Ge-Se bonds at this point. E_d is a measure of inter-band transitions, and the decrease in E_d with either Ge or Ga is most likely an indication of decreasing interconnectivity in the first coordination shell [38]. Ultimately, refractive index is dependent on both E_0 and E_d and appears to be strongly affected by both the composition's chemical ordering and topological structure.

4.3. Heat capacity and thermal conductivity

Debye theory (see Appendix A) has been used to explain the increase in heat capacity with coordination number. An integral-free expression based on measured acoustic velocities, polylogarithms, and the Riemann zeta function is shown below [39],

$$c_v(T) = 3Nk_B\{DC_k(x)\} \tag{12}$$

where N is Avogadro's number, k_B is the Boltzmann constant, and $DC_k(x)$ is the Debye function with $x = \frac{\theta_D}{T}$. Eq. (12) indicates that all specific heat values, c_v, should be a function of the material's Debye temperature with specific heat increasing with increasing θ_D. The fact that no maximum is observed at $< r > = 2.67$ indicates that the trends in heat capacity are not dominated by bond energy (i.e. chemical ordering) alone, as this point would have the highest ratio of Ge(Ga)—Se bonds with the largest bond energy. Therefore, the increase in heat capacity from $< r > = 2.3$ to $< r > = 2.6$ is most likely due to topological effects resulting from the removal of the chain like Se—Se structure and addition of Ge(Ga)—Se bonds in tetrahedral $GeSe_2$ and $GaSe_2$ units. The continued increase in the heat capacity past $< r > = 2.67$ is due to the addition of Ge(Ga)—Ge(Ga) cage-like units. The bond energy for this homopolar bond is less than that of the heteropolar Ge(Ga)—Se bond, which leads to reduced vibrational velocities as show in Table 3. If this were the only factor, one would expect to see reduced heat capacities at this point, but the greater packing efficiency of these units leads to higher densities (see Part I), which is what ultimately leads to increased Debye temperatures (Eq. (A-7)) and further increases in heat capacity (Eq. (A-8/10)). Therefore, it has been shown both experimentally and from a first principles model that the heat capacity is predominantly driven by topological structure and that increased crosslinking leads to higher heat capacities.

Kinetic gas theory can be used to understand phenomenologically both the property and structure relationships of thermal conductivity as shown in Eq. (13) [40,41],

$$k_T = \sum_{i=e,p,l} \frac{1}{3} c_i v_i \lambda_i \rho \tag{13}$$

where c_i is the heat capacity, v_i is the carrier velocity, λ_i is the mean free path of the carrier, and ρ is the bulk density. In this model, the chemical ordering (i.e., average bond strength) will primarily affect v_i, and topological ordering will control the time between scattering events which correlates to λ_i. Therefore, there is a direct or linear effect of each on the total thermal conductivity. As the composition moves across < r > = 2.4, the Ge_x-Ga_y-Se_{1-x-y} structure transitions from one dominated by 1-D Se—Se chains to a 2-D structure dominated by Ge(Ga)Se_2 tetrahedral units. At this point, the chemical ordering (directly related to average bond strength) increases, leading to an increase in v_i. In addition, the 2-D structure is more ordered and will lead to less phonon scattering, thereby increasing the mean free path of the phonon carriers, λ_i. As the composition moves across < r > = 2.67, the structure becomes Se-deficient, meaning that the 1-D Se—Se chains disappear, and the presence of 3-D crosslinked network containing (Ga)—Ge(Ga) bonds appears. The Ge(Ga)—Ge(Ga) bonds have a lower mean bond energy than the Ge(Ga)—Se bonds, which should lead to decreased v_i. Therefore, the continued increase in thermal conductivity must be due to an increase in λ_i caused by a reduction in phonon scattering events. The balance between carrier velocity (v_i) decrease and mean free path (λ_i) increase is what causes the small inflection at this point. Regardless of the exact nature of the carrier transport, Ge_x-Ga_y-Se_{1-x-y} glasses show

an increase in heat conduction with the addition of increasing dimensionality to the structural units comprising the glass.

This large variation in lattice thermal conductivity suggests that the glasses examined within the Ge_x-Ga_y-Se_{1-x-y} series undergo large topological and chemical changes in moving from Se-rich to Se-deficient compositions. The peak lattice thermal conductivity, $< r > = 2.8$, correlates to Se-deficient compositions which are predominantly metal-metal heteropolar bonded tetrahedral $Ge(Ga)Se_2$ structures with the emergence of cage like Ge(Ga)—Ge(Ga) bonding. If bond strength was the primary driving force for lattice thermal conductivity, we would expect to see a peak at $< r > = 2.67$ corresponding to a predominantly homogenous Ge(Ga)—Se bonds. Therefore, $Ge_xGa_ySe_{1-x-y}$ glasses show an increase in lattice conduction with the addition of increasing dimensionality originating from the structural units comprising the glass.

The large fraction of photon thermal conductivity found at room temperature in all $Ge_xGa_ySe_{1-x-y}$ glasses is in part due to the weak bonding and low phonon vibrational frequencies found in chalcogenides, leading to some of the lowest lattice thermal conductivity values found in any material [42,43]. This is an indication that photonic thermal conduction is driven by chemical ordering, which is further supported by the large inflection at the chemical transition threshold $< r > = 2.67$. For a given Ga concentration and optical frequency (in this case $\lambda = 4.515\,\mu m$), as average bond strength increases, both refractive index and optical absorption of incident electromagnetic radiation decrease (the one exception to this trend is $Ge_{0.3}Ga_{0.1}Se_{0.6}$). There is also the possibility the gas kinetic theory assumptions used to derive Eq. (A-2) played a role in the discrepancy between photon and lattice conduction. The assumption of a single refractive index and absorption coefficient for a given composition is limiting. For instance, comparisons between sulfur- and selenium-based chalcogenides are probably invalid as the model does not take into account the width of the optical transmission band, simply the average absorption coefficient over all optical wavelengths measured. Fortunately, most of the glasses in this study exhibited a similar optical transmission regime. This limitation in the optical wavelengths measured could have also lead to the removal of impurity based effects. As stated previously, the photonic conduction calculations were determined from optical measurements strictly at $\lambda = 4.515\,\mu m$, which was outside of any observed optical impurity absorption bands, whereas the lattice thermal conductivity was determined by subtraction of the calculated photonic conductivity and the measured total thermal conductivity. It is possible that impurities have led to a greater reduction in overall measured thermal conductivity than the photonic at a single wavelength, which would decreased the lattice thermal conductivity calculations to a greater degree than the photonic conductivity calculations. Regardless of the limitations of the model, the high percentage of photonic thermal transport calculated at room temperature is most likely real phenomena due to the extremely weak lattice conduction mechanism as well as the large infrared transmissivity of $Ge_xGa_ySe_{1-x-y}$ glasses.

5. Conclusions

Ten crystal-free compositions from 10 to 30 mol% Ge and 5 to 15 mol% Ga were melt-quenched, and their thermal (glass transition temperature, heat capacity, thermal conductivity) and optical (band edge absorption, average absorption in transmission window, refractive index) properties were measured and compared, to assess trends with average coordination number $< r >$ and average bond strength $< E >$. For Se-rich compositions that can be generally considered to be polymeric with Se chains connecting Ge(Ga)—Se structural units, thermal property values increased with increasing coordination. Correlation between structure and properties was less clear for higher coordination numbers around $< r > = 2.67$, in which the composition became increasingly cross-linked, Se deficient, and the emergence of Ge(Ga)—Ge(Ga) cage-like units was detected. Refractive index, glass transition temperature, and band gap all showed sharp inflections around $< r > = 2.67$. These properties are most likely dominated by bond strength were the highest fraction of Ge(Ga)—Se bonds, which have the high bond energy, are found at this point. Thermal conductivity and heat capacity increased through the $< r > = 2.67$ threshold, indicating a strong dependence on the topological network of the glass, in which continued crosslinking and interconnectivity lead to increased magnitude of these properties.

Heat capacity and photonic thermal conductivity were estimated by theoretical models. Photonic conductivity was shown to comprise the dominant portion of room temperature thermal conductivity, contributing ~30 to 65% of the total thermal conductivity.

Ultimately, this was the first study to thoroughly investigate the thermal (Part II, this work), optical (Part II, this work), and mechanical (Part I) properties of the glass forming region of the $Ge_xGa_ySe_{1-x-y}$ ternary. Employing this complementary approach to correlate the compositional impact of structure on properties enables a more complete interpretation of properties based on both calculated and experimentally derived data.

Acknowledgments

This research was supported in part with funding from the Defense Threat Reduction Agency (DTRA) under Contract No HDTRA1-13-0001. The authors would also like to acknowledge Dr. Anupama Yadav for collecting UV–Vis and XRD data (not shown) that was used in the development of this paper.

Appendix A. Theory in thermal properties

Three independent carrier mechanisms are responsible for thermal energy transport in a solid material. Therefore, total thermal conductivity, k_T, is a summation of lattice (k_l), photon (k_p), and electron (k_e) carrier components:

$$k_T = k_p + k_l + k_e \tag{A-1}$$

Phonon transport is determined by the glass lattice's atomic bonds, electron transport is determined by free electron carriers, and photon transport is determined by the electron clouds response to electromagnetic radiation [40,41,44]. In order to determine the electron fraction contribution, k_e, to the total thermal conductivity, k_T, the Wiedemann-Franz law with the theoretical Lorenz number was used. $Ge_xGa_ySe_{1-x-y}$ compositions are amorphous semiconductor with electrical conductivities in the range of $\sim 10^{-11}\,\Omega\cdot cm$ at 300 K [45]. Therefore, the electronic portion of thermal conductivity, k_e, was assumed to be very small, near $10^{-19}\,W/m\cdot K$. Due to this, the electronic contribution has been ignored in the present analysis, leaving just photon and lattice thermal conductivity. A simple equation for photon conduction, k_p, can be derived from gas kinetic theory as shown in Eq. (A-2) [46,47]

$$k_p = \left(\frac{16}{3}\right)\frac{\sigma_{SB} n^2 T^3}{\alpha} \tag{A-2}$$

where σ_{SB} is the Stephan-Boltzmann constant, n is the refractive index, T is the temperature, and α is the absorption coefficient for the material. Using Eq. (A-2), photon thermal conductivity can be calculated with measurements of total thermal conductivity, average absorption coefficient, and refractive index over the transmissive regime. If k_e is ignored, k_l can then be determined mathematically using Eq. (A-1).

Specific heat, c_v, can be derived from Debye's model of the phonon spectrum and Slack's model for high temperature ($T > \theta_D$) thermal conductivity [41,48–53]. The Debye theory assumes that a linear relation exists for all phonon frequencies, $\omega(q,s)$, where q is an index which refers to the wave number and s is an index which refers to the phonon mode. A constant value $C(q,s) = C_D$ is assumed such that the Debye frequency is equivalent to Eq. (A-3) (from Ref. 41) where ν_D is the ordinary Debye frequency.

$$\omega_d = (C_D)q_D = 2\pi\nu_D \tag{A-3}$$

Derivations of the Debye wave number, q_D, lead to the following equivalent expressions, when using either the ω_D or ν_D respectively,

$$q_D = (6\pi^2 N/V)^{1/3} = (3\rho N_A r/4\pi\overline{M})^{1/3} \tag{A-4}$$

where N is the number of atoms per unit volume, V is the crystal volume, r is the number of atoms in the molecule, $\overline{M}$ is the average molecular weight, N_A is Avogadro's number, and ρ is the density. Acoustic waves in a real solid are anisotropic, and there are different constants for both longitudinal, C_L, and transverse, C_T, acoustic branches which can be related to C_D through the following Equation.

$$\frac{3}{c_D^3} = \frac{1}{c_L^3} + \frac{1}{c_T^3} \tag{A-5}$$

The Debye temperature is a measure of the maximum phonon frequency,

$$\theta_D = \frac{h\omega_D}{k_B} \tag{A-6}$$

where h is Planck's constant, and k_B is the Boltzmann's constant [48]. Utilizing Eqs. A-3 through A-6, the Debye temperature can be derived as shown in Eq. (A-7) [51]

$$\theta_D = \frac{h\omega_D}{k_B} = \frac{h}{k_B}\left(\frac{3\rho N_A r}{4\pi\overline{M}}\right)^{1/3}\left(\frac{(1/C_L^3) + (2/C_T^3)}{3}\right)^{-1/3} \tag{A-7}$$

Dubinov and Dubinova have developed an exact explicit integral-free expression for the integral Debye function found in the solution of the Debye heat capacity theory [39]. The integral Debye function for heat capacity with $x = \frac{\theta_D}{T}$ is defined as follows.

$$\theta_D \simeq DC_k(x) = \frac{k}{x^k}\int_0^x \frac{t^{k+1}\exp(-t)dt}{[1-\exp(-t)]^2} \tag{A-8}$$

Using the Riemann zeta function, $\zeta(x)$, and polylogarithms, $Li_V(x)$, a finite sum for the integral in Eq. (A-8) can be expressed as follows.

$$DC_k(x) = \frac{k}{x^k}\left\{(k+1)!\zeta(k+1) - \sum_{m=0}^{K+1}\frac{(k+1)!}{m!}x^m Li_{k-m+1}[\exp(-x)]\right\} \tag{A-9}$$

Finally, for $k = 3$ (3 dimensional heat transfer), Eq. (A-9) can be written as follows

$$DC_3(x) = \frac{4}{5}\frac{\pi^4}{x^3} + \frac{3x\exp(-x)}{[\exp(-x)-1]} + 12\ln[1-\exp(-x)] - \frac{36}{x}Li_2[\exp(-x)] - \frac{72}{x^2}Li_3[\exp(-x)] - \frac{72}{x^3}Li_4[\exp(-x)] \tag{A-10}$$

Therefore, with experimental or computational measurements of C_L, C_T, and ρ, one can calculate the thermophysical properties θ_D(A-8) and c_v can be calculated based on Eq. (A-11).

$$c_v(T) = 3Nk_B\{DC_k(x)\} \tag{A-11}$$

Appendix B. Selenium deficiency

Selenium deficiency (S), is defined such that stoichiometric composition (i.e., a 1:1 ratio of Ge(Ga) to Se) would give a zero value, a Se-deficient composition would give a negative value, and a Se-rich composition gives a positive value as shown below,

$$S = 1 - \left(\frac{2(1-x-y)}{4x+4y}\right) \tag{A-12}$$

where x, y represent the respective atomic fraction of Ge and Ga in the given $Ge_xGa_ySe_{1-x-y}$ composition.

References

[1] A. Giridhar, S. Mahadevan, J. Non-Cryst. Solids 126 (1990) 161.
[2] G. Yang, T. Gueguen, J.-C. Sangleboeuf, T. Rouxel, C. Boussard-Pledel, J. Troles, P. Lucas, B. Bureau, J. Non-Cryst. Solids 377 (2013) 54.
[3] A.W. Mao, B.G. Aitken, R.E. Youngman, D.C. Kaseman, S. Sen, J. Phys. Chem. B 117 (2013) 16594.
[4] M. Zhu, Q. Nie, X. Wang, S. Dai, X. Zhang, X. Sehn, G. Wang, X. Lv, Spectrochim. Acta A 75 (2010) 1275.
[5] Sudha Mahadevan, A. Giridhar, J. Non-Cryst. Solids 152 (1993) 42.
[6] M.F. Thorpe, D.J. Jacobs, M.V. Chubynsky, J.C. Phillips, Journal of Non-Crystalline Solids, 266–269 B (2000), p. 859.
[7] J.C. Phillips, M.F. Thorpe, Solid State Commun. 53 (1985) 699.
[8] J.C. Phillips, Phys. Status Solidi B 101 (1980) 473.
[9] J.C. Phillips, J. Non-Cryst. Solids 34 (1979) 153.
[10] A.K. Varshneya, A.N. Sreeram, D.R. Swiler, Phys. Chem. Glasses 34 (1993) 179.
[11] R. Golovchack, L. Calvez, E. Petracovschi, B. Bureau, D. Savytskii, H. Jain, Mater. Chem. Phys. 128 (2013) 909.
[12] M. Roze, L. Calvez, Y. Ledemi, M. Allix, G. Matzen, X.-H. Zhang, J. Am. Ceram. Soc. 91 (2008) 3566.
[13] L. Tichy, H. Ticha, J. Non-Cryst. Solids 189 (1995) 141.
[14] J. Lonergan, C. Lonergan, J. McCloy, K.A. Richardson, J. Non-Cryst. Solids (2019).
[15] J.R. Taylor, An Introduction to Error Analysis: The Study of Uncertainties in Physical Measurments, 2nd ed, University Science Books, Sausalito, California, 1997.
[16] Peter Krupa, S. Malinaric, Int. J. Methem. Comput. Phys. Electr. Comput. Eng. 8 (2014).
[17] B. Gleason, Thesis, Clemson University, 2015.
[18] N. Carlie, N.C. Anheier Jr., H.A. Qiao, B. Bernacki, M.C. Phillips, L. Petit, J.D. Musgraves, K. Richardson, Rev. Sci. Instrum. 82 (2011) 052103.
[20] X. Zhang, H. Ma, J.-L. Adam, J. Lucas, G. Chen, D. Zhao, Mater. Res. Bull. 40 (2005)

1816.
[21] B. Ye, S. Dai, R. Wang, G. Tao, P. Zhang, X. Wang, X. Shen, Infrared Phys. Technol. 77 (2016) 21.
[22] E. Marquez, J.M. Gonzalez-Leal, A.M. Bernal-Oliva, T. Wagner, R. Jimenez-Garay, J. Phys. D. Appl. Phys. 40 (2007) 5351.
[23] J. Tauc, Amorphous and Liquid Semiconductors, Plenum Press, New York, 1974.
[24] S.-C. Liu, Y. Mi, D.-J. Xue, Y.-X. Chen, C. He, X. Liu, J.-S. Hu, L.-J. Wan, Adv. Electron. Mater. 3 (2017) 1–7.
[25] A.A. Otham, K.A. Aly, A.M. Abousehly, Thin Solid Films 515 (2007) 3507.
[26] K.J. Rao, R. Mohan, Solid State Commun. 39 (1981) 1065.
[27] N. Mott, E. Davis, Electronic Process in Non Crystalline Materials, 2nd Edition ed. University Press, Oxford, 1979.
[28] G. Lucovsky, Phys. Rev. B 15 (1977) 5762.
[29] K. Tanaka, Phys. Rev. B 39 (1989) 1270.
[30] W.-H. Wei, R.-P. Wang, X. Shen, L. Fang, B. Luther-Davies, J. Phys. Chem. C 117 (2013) 16571.
[31] G. Saffarini, J.M. Saiter, J. Mater. Sci. 39 (2004) 6141.
[32] T. Wagner, S.O. Kasap, K. Maeda, J. Mater. Res. 12 (1997) 1892.
[33] I. Pethes, V. Nazabal, R. Chahal, B. Bureau, I. Kaban, S. Belin, P. Jovari, J. Alloys Compd. 673 (2016) 149.
[34] V. Gurin, O. Shpotyuk, and V. Boyko, (arXiv:1304.1251 [cond-mat.mtrl-sci], 2013), p. 1.
[35] T.G. Edwards, S. Sen, E.L. Gjersing, J. Non-Cryst. Solids 3 (2012) 609.
[36] S.H. Wemple, Phys. Rev. B 7 (1973) 3767.
[37] S.H. Wemple, M. DiDomenico Jr., Phys. Rev. B 3 (1971) 1338.
[38] J.S. McCloy, B.J. Riley, S.K. Sundaram, H.A. Qiao, J.V. Crum, B.R. Johnson, J. Non-Cryst. Solids 356 (2010) 1288.
[39] A.E. Dubinov, A.A. Dubinova, Tech. Phys. Lett. 34 (2008) 999.
[40] T.M. Tritt, Thermal Conductivity (Theory, Properties, and Applications), Kluwer Academic / Plenum Publishers, New York, 2004.
[41] G. Grimvall, Thermophysical Properties of Materials, (Elsevier, Amsterdan, The Netherlands, 1999.
[42] M. Burzo, P. Komarov, P. Raad, IEEE CPMT 26 (2003) 80.
[43] A. Delan, M. Rennau, S.E. Shulz, T. Gessner, Microelectron. Eng. 70 (2003) 280.
[44] J.R. Howell, R. Siegel, Thermal Radiation Heat Transfer, Third ed, Hemisphere Publishing Corporation, Washington, DC, 1992.
[45] G.J. Adriaenssens, A. Gheorghiu, C. Senemaud, N. Qamhieh, N. Bolle, E. Sleeckx, P. Nagels, J. Non-Cryst. Solids 198-200 (1996) 675.
[46] M. Zhao, X. Ren, W. Pan, J. Eur. Ceram. Soc. 35 (2015) 1055.
[47] W.D. Kingery, H.K. Bowen, D.R. Uhlmann, Introduction to Ceramics, John Wiley & Sons Inc, New Tork, 1960.
[48] Donald T. Morelli, G.A. Slack, Subhash L. Shinde, J.S. Geola (Eds.), High Thermal Conductivity Materials, Springer, New York, 2006.
[49] D.V. Schroeder, An Introduction to Thermal Physics, Addison-Wesley, 2000.
[50] C. Kittel, Introduction to Solid State Physics, 7th ed., Wiley, 1996.
[51] D. Bridge, A.A. Higazy, J. Mater. Sci. 21 (1986) 2385.
[52] G.A. Slack, Solid State Phys. 34 (1979) 1.
[53] C.L. Julian, Phys. Rev. 113 (1965) 1046.